Available online at www.sciencedirect.com
ScienceDirect
Trans. Nonferrous Met. Soc. China 32(2022) 2908−2921
Transactions of Nonferrous Metals Society of China
www.tnmsc.cn

Effects of annealing treatments on forming performance of zirconium alloys

Cong-yi LEI[1,2], Jian-zhong MAO[1,2], Dian-wu ZHOU[1,2], Xiao-min ZHANG[1,2], Lian WANG[3]

1. State Key Laboratory of Advanced Design and Manufacturing for Vehicle Body, Hunan University, Changsha 410082, China;
2. College of Mechanical and Vehicle Engineering, Hunan University, Changsha 410082, China;
3. State Nuclear Bao-Ti Zirconium Industry Company, Baoji 721000, China

Received 9 July 2021; accepted 17 March 2022

Abstract: The effects of annealing treatments (ATs) on the microstructure of Zr−Sn−Nb alloy strips were studied. Based on the characteristics of strips for nuclear fuel assemblies, punching experiments were carried out and the formability of zirconium alloy strips was quantitatively evaluated. The results indicate that the proportions of small-angle grain boundaries of the zirconium alloy under conditions of annealing treatment at 580 °C (AT I) and annealing treatment at 620 °C (AT II) are 14.3% and 23.2%, respectively, while that of the as-received material is 12.4%. And the forming limit margin fields of the zirconium alloy under AT I can reach 0.43%, while the values of the as-received material and the AT II are −0.35% and −2.8%, respectively. The annealing process affects the evolution process of the strip recrystallization texture and the grain size. Moreover, the total texture and pole density are closely related to the degree of anisotropy of the strip. Besides, the small-angle grain boundary affects the strain path and crack expansion of the necking unit during the strip punching process, while the grain size affects the hardening exponent of the material.

Key words: forming performance; zirconium alloys; annealing process; strain path; forming limit; texture

1 Introduction

Zirconium alloy has been widely used as the fuel cladding and strips of spacer grid's structure material due to its outstanding low absorption cross section for thermal neutrons, strong corrosion resistance and acceptable toughness in the irradiation environment [1−6]. At present, the high-speed punching is mainly used as a production method of strips in the nuclear fuel assembly. However, due to the poor formability and obvious anisotropy of zirconium alloys, the forming process of strips often fails because of cracks in actual production. The improvement of the forming performance of zirconium alloys is closely related to the cost of strip manufacturing as well as the safety and operation stability of nuclear fuel assemblies.

Annealing treatment (AT) can be considered as an effective method to modify properties of metals by altering the microstructure [7,8] such as recrystallization [9,10], grain growth [11,12] and phase transformation [13,14]. It has been demonstrated that the tensile strength and yield strength of E125 zirconium alloy can be significantly enhanced by high-pressure torsion (HPT) and subsequent annealing treatments due to the grain growth and phase transformation [15]. HE et al [16] studied the effects of the loading direction

Corresponding author: Jian-zhong MAO, E-mail: maojianzhong66@163.com; Dian-wu ZHOU, E-mail: ZDWe_mail@126.com
DOI: 10.1016/S1003-6326(22)65992-2

on the deformation and subsequent annealing treatments at different temperatures on the texture-dependent recrystallization behavior of Zr-4 alloy. TIAN et al [17] have presented the relationship between the recrystallization behavior of cold-rolled Zr−1Nb alloy and the corresponding deformation reductions as well as annealing temperatures. The results show that the recrystallization process of Zr−1Nb alloy can be accelerated by large deformation amount and high annealing temperature.

ZHANG et al [18] have studied the mechanical properties, electrical conductivity as well as the evolution of microstructure of Cu−0.15Zr alloy during elevated-temperature annealing. They claim that the specific alloy displays outstanding comprehensive mechanical property after high temperature annealing. TIAN et al [19] have explained the effects of annealing on the mechanical properties of the Mg−Nd−Zn−Zr magnesium alloy through the methods of microscopic observations and tensile tests. They found that more precipitates of secondary phases could be acquired under a lower annealing temperature and longer annealing time. KAMALI et al [20] have discussed the impact of various annealing treatment temperatures and holding time on the microstructure and the corresponding mechanical properties of the cold-rolled Fe−Co−10V alloy. From this study, it can be known that the hardness and the yield strength as well as the elongation of material have close relationship with the annealing temperature. As for studying the effects of the annealing treatments on the microstructure and properties of hot compressed Au80Sn20 alloy, HUANG et al [21] found that the microstructure of the specific alloy developed from lamellar to equiaxed grains and the grains could grow significantly with a higher annealing temperature while the grain orientation is more uniform.

Many studies have discussed the effects of annealing or heat treatment on the microstructures and mechanical properties such as tensile strength, yield strength or microhardness of zirconium alloys or other alloys. But there are limited data reported about the formability improvement of the zirconium alloy. Since the forming performance of zirconium alloys is considered as one of the most crucial indexes during the manufacturing process of the grid spacer strip of the nuclear fuel assembly, it is necessary to discuss the effects and the corresponding mechanisms of the annealing treatments on the forming performances of the zirconium alloys under a quantifiable system. In this study, a new Zr−Sn−Nb zirconium alloy was annealed at temperatures of 580 and 620 °C, respectively. The forming performances of the zirconium alloy specimens under different ATs were evaluated by the strip stamping experiments. The mechanisms of how the annealing treatments affect the forming performances of the zirconium alloys were discussed from both the macro perspective and the micro perspective. The forming limit curves of the zirconium alloys under different annealing treatments were analyzed based on the MK-Barlart method through theoretical calculations. Moreover, the strain paths and the forming limit margin fields of the necking element of the clamping rigidity convexity structure used in the strips of nuclear fuel assembly were studied by finite element method. At last, the microstructures and textures of the materials were observed and analyzed through a scanning electron microscope (SEM) equipped with the electron back scatter diffraction (EBSD) detector.

2 Experimental

2.1 Annealing treatments

The material used in this investigation was a Zr−Sn−Nb zirconium alloy with the thickness of 0.457 mm and the nominal composition [22] of Zr−0.5Sn−0.5Nb−0.3Fe−0.015Si. The as-received material was a commercial zirconium alloy industrially fabricated by rolling and annealing, while the as-rolled state of the as-received material was annealed in different conditions. To prevent the samples from being oxidized due to the heat treatments in air, the following annealing tests were conducted in a vacuum furnace. Considering the size of the vacuum furnace and the subsequent stamping tests, the annealing samples were sliced as 52 mm (RD) × 72 mm (TD) from the as-rolled sheet of the alloy. The annealing temperatures of 580 and 620 °C were selected respectively with a fixed heating rate of 5 °C/ min while the holding time for each of the heat treatment was set to be 2 h. To distinguish the specimens under different annealing treatments, the one with the annealing

temperature of 580 °C was noted as AT I, while the other with a higher annealing temperature (620 °C) was noted as AT II.

2.2 Stamping experiments

As mentioned above, zirconium alloys are mainly applied as the structure material of the spacer gird strip in the PWR nuclear power plants. Therefore, to evaluate the effects of different annealing treatments on the stamping formability of the Zr−Sn−Nb zirconium alloys intuitively, a specific structure of the strip named clamping rigidity convexity shown in Fig. 1 was selected and the stamping experiments were conducted by a self-designed mold. To ensure the objectivity and fairness of the stamping experiments, the zirconium alloys under different AT conditions (AT I and AT II) were compared under the exactly same boundary conditions in the stamping tests, during which the punch speed was set to be 76 mm/s and the blank holder force to be 50 kN. In addition, considering the comprehensiveness of the stramping tests, for each set of zirconium alloy, nine stamping tests were conducted and the results were illustrated from Fig. 2 to Fig. 4.

From Fig. 2, it can be clearly observed that for the as-received zirconium alloy, two rigidity convexities, the coordinates of which are (1,1) and (3,3) respectively, have been cracked among the nine stamping experiments. Besides, the other three rigidity convexities, noted as (1,3), (3,1) and (3,2) in Fig. 2, are in the critical region of cracking and uncracking, meaning that these three rigidity

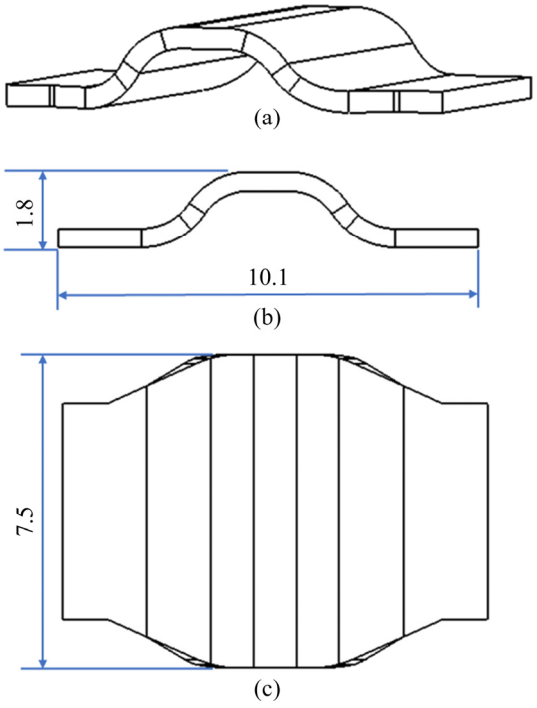

Fig. 1 Geometry structure (a) and nominal dimensions (b, c) of clamping rigidity convexity (unit: mm)

convexities have relatively high risk of cracking during the forming process.

Figure 3 displays the stamping results of the Zr−Sn−Nb zirconium alloy under AT I. Compared with the as-received material, no obvious cracks are found among the nine stamping tests of the samples under AT I, but there are still three rigidity convexities in the critical region of cracking and uncracking, noted as (2,2), (3,1) and (3,3) respectively in Fig. 3. Among them, the one named

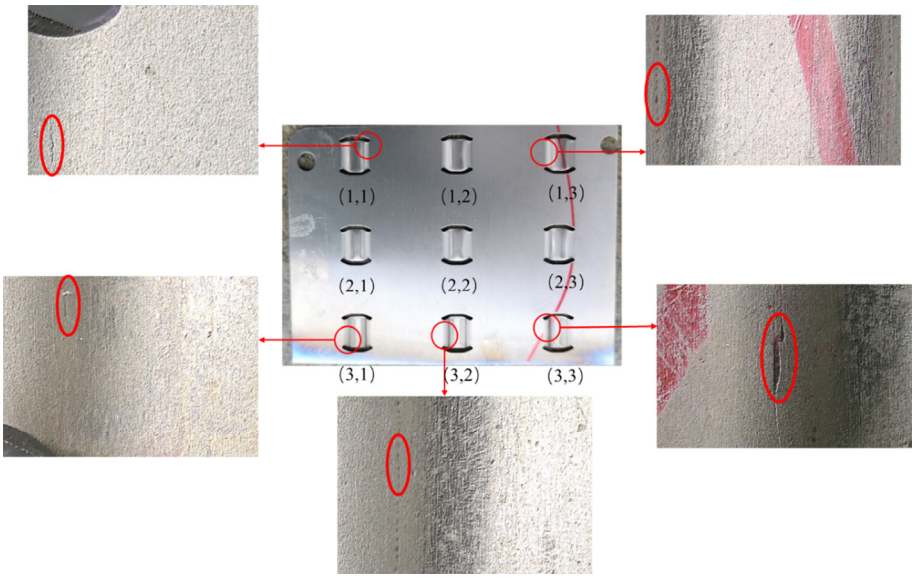

Fig. 2 Stamping results of as-received zirconium alloy

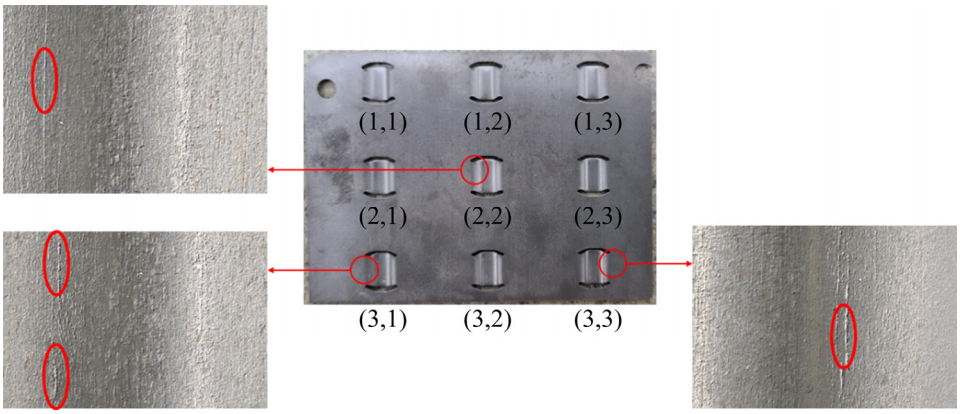

Fig. 3 Stamping results of zirconium alloy under AT I

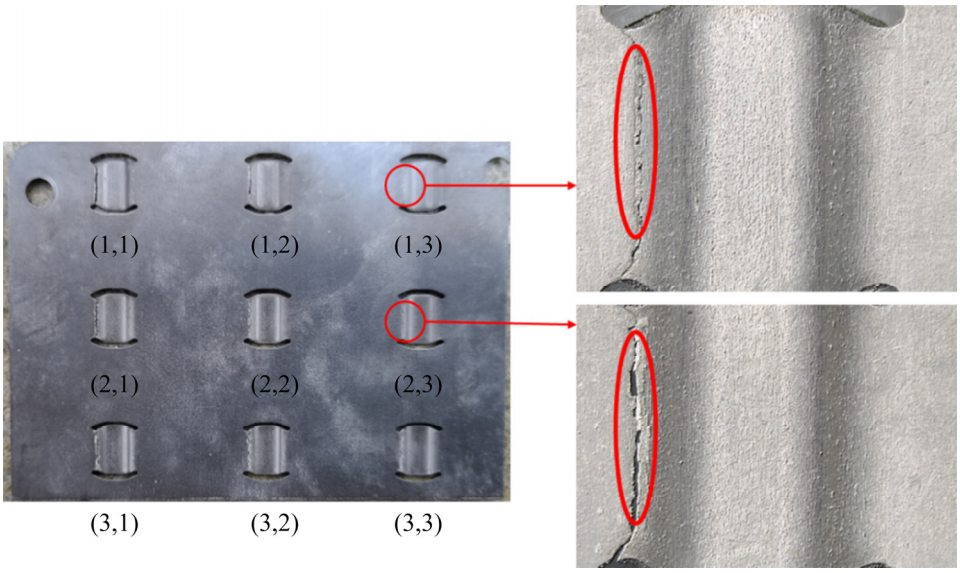

Fig. 4 Stamping results of zirconium alloy under AT II

(3,3) has higher risk of cracking. As for the zirconium alloy under AT II with the formability displayed in Fig. 4, it can be seen that all the nine rigidity convexities are cracked. Compared with the previous stamping experiments, the cracks of the zirconium alloy under the AT II are much more obvious and degree of the cracking is intenser.

The stamping results of the as-received zirconium alloy and those under AT I and AT II are summarized in Table 1. It can be derived from Table 1 that compared with the as-received material and the one under AT II, the Zr−Sn−Nb zirconium alloy under AT I has displayed a better formability during the rigidity convexity stamping tests. The mechanisms of how the annealing treatment affects the formability of the Zr−Sn−Nb zirconium alloy were discussed as follows from both macro perspective and micro perspective.

Table 1 Stamping tests of three sets of zirconium alloys

Material	Crack	Critical region	Safety region
As-received	2	3	4
AT I	0	3	6
AT II	9	0	0

2.3 Microstructure observations

To further discuss the effect of annealing process on the formability of the material, the microstructures and textures of the materials were observed by a Zeiss EVO MA10 SEM equipped with the EBSD detector. Samples used in this study were polished mechanically and electrochemically and the data of the observations by the EBSD equipment were collected with a step of 0.6 μm.

3 Numerical approach and analysis

To reveal the effect of the annealing treatments on the forming performances of the zirconium alloys, the forming limit curves (FLCs) of the three zirconium alloys under different annealing conditions are calculated based on MK-Barlat method, the strain paths of the materials are discussed through finite element analysis.

3.1 Forming limit curve

The concept of FLC was firstly proposed by GENSAMER [23] and BANABIC et al [24], then developed by KEELER [25,26] and GOODWIN [27]. In recent years, the FLC has been widely adopted in the field of sheet metal forming as a crucial index to evaluate the forming performance of materials and the crack predictions [28,29]. Figure 5 illustrates what the FLC looks like defined in Ref. [30]. Based on the definition of the FLC, the region above the FLC (red line in Fig. 5) is considered as the crack area during the forming process; the region below the FLC indicates that there is no crack risk during the plastic deformation. The strain points just located on the red line are in the critical area of the crack and non-crack.

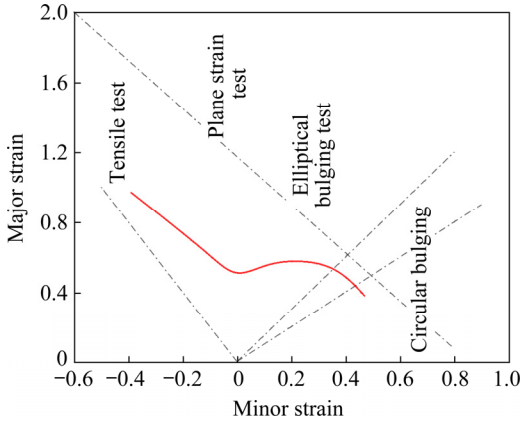

Fig. 5 FLC of material defined in Ref. [30]

FLC can be determined by both experiments and theoretical calculations. However, given the time and cost (especially the price of zirconium alloys) needed by the experiment method and its strict requirement on the geometric dimensions of the test samples, several models have been developed to obtain the FLCs of the material by theoretical method. In this study, in order to evaluate the forming performances of the Zr−Sn−Nb zirconium alloys with different treatments, FLC was employed and determined by theoretical calculations. The theoretical calculations were proved with enough accuracy by many literatures and the calculation method used in this study was also verified by Nakajima tests introduced in detail in author's previous work [31].

Since the zirconium alloys are anisotropic, to get an accurate calculation result of the FLC, the modified Marcinia−Kuczyński (M−K) model with an initial inclination and Barlat 89 anisotropic criterion were employed to predict the forming performances of the materials. M−K model was firstly introduced by MARCINIAK and KUCZYŃSKI [32] in 1967 with the assumption that the instable conditions occurred due to the initial imperfection in the material, and then developed by HUTCHINSON et al [33,34] who presumed an inclination of the imperfection on the original M−K model shown in Fig. 6. In Fig. 6, t_0^A and t_0^B are the initial thicknesses of Regions A and B, respectively, while f_0 is defined as the ratio of the initial uniform thickness of the two areas. The three basic hypotheses of M−K model are shown as follows.

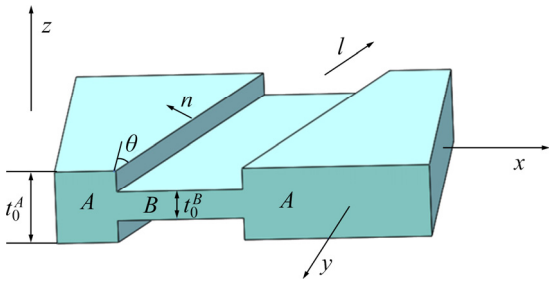

Fig. 6 Geometry schematic diagram of M−K model

(1) Force balanced equation:

$$\sigma_{nn}^A t^A = \sigma_{nn}^B t^B \tag{1a}$$

$$\sigma_{nl}^A t^A = \sigma_{nl}^B t^B \tag{1b}$$

where σ_{nn}^A and σ_{nn}^B are shear stresses of Regions A and B along nn direction, respectively; t^A and t^B are the instantaneous thicknesses of Regions A and B during the deformation, respectively; σ_{nl}^A and σ_{nl}^B are shear stresses of along nl direction, respectively.

(2) Volume invariant during the deformation:

$$d\varepsilon_{xx}+d\varepsilon_{yy}+d\varepsilon_{zz}=0 \tag{2}$$

where $d\varepsilon_{xx}$, $d\varepsilon_{yy}$ and $d\varepsilon_{zz}$ are strains in xx, yy and zz directions, respectively.

(3) Deformation continuity of the groove:

$$\Delta\varepsilon_{ll}^{A}=\Delta\varepsilon_{ll}^{B} \tag{3}$$

where ε_{ll}^{A} and ε_{ll}^{B} are strains of Regions A and B along ll direction, respectively.

To describe the anisotropic yield behavior of zirconium alloys during the predictions of the forming limit curve, Balart 89 criterion [35] which considered the planar anisotropy and introduced shear stress was employed and shown as follows:

$$f=a\left|k_1+k_2\right|^{M}+a\left|k_1-k_2\right|^{M}+c\left|2k_2\right|^{M}=2\sigma_{\mathrm{e}}^{M} \tag{4}$$

where a and c are material constants, M is the crystallographic-structure exponent of the material [36,37], σ_{e} is the effective stress, and parameters k_1 and k_2 can be calculated by Eqs. (5) and (6):

$$k_1=\frac{\sigma_{xx}+h\sigma_{yy}}{2} \tag{5}$$

$$k_2=\left[\left(\frac{\sigma_{xx}-h\sigma_{yy}}{2}\right)^{2}+p^{2}\sigma_{xy}\right]^{1/2} \tag{6}$$

where h and p are the material parameters, σ_{xx}, σ_{yy} and σ_{xy} are stresses in xx, yy and xy directions, respectively.

Combining with the M−K model and Barlat 89 criterion, the FLC of material can be calculated by a self-programmed code based on Matlab 2016b, with the calculation procedure illustrated in Fig. 7. To

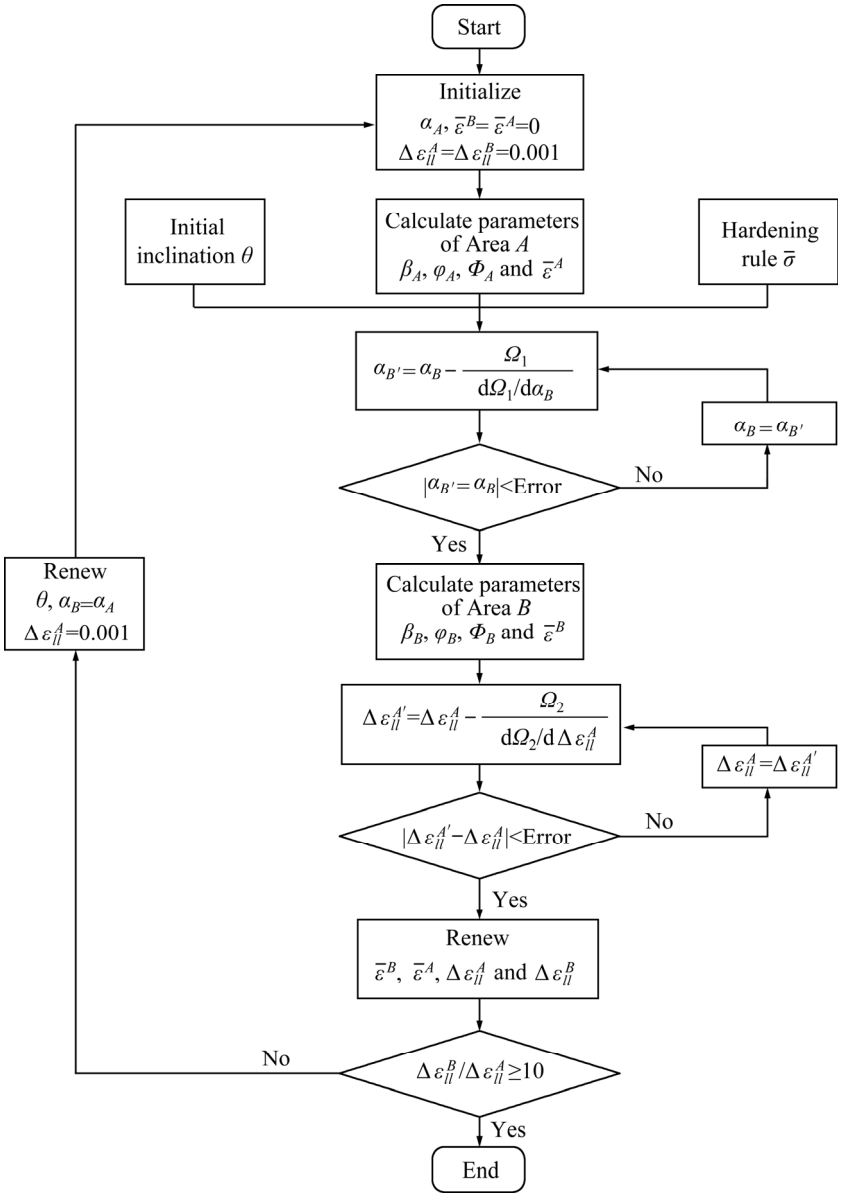

Fig. 7 Iteration procedure of FLC

improve the calculation accuracy of the FLCs of the zirconium alloys (close-packed-hexagonal structure), the crystallographic-structure exponent M in this study was set to be 8, while the extended detailed derivation was discussed in the author's previous study [31]. The parameters such as β, φ and Φ are the intermediate variables which can be obtained by the basic mechanical properties through tensile tests. To calculate the crucial parameters used in Barlat 89 criterion, tensile tests of the zirconium alloys under different annealing treatments were conducted by a Zwick/Roell Z010 tensile machine with a digital image correlation (DIC) system to capture the strains during the tests. The geometry dimensions of the tensile samples are illustrated in Fig. 8. For each of the zirconium alloy, the tensile tests were conducted along three directions (TD, RD and 45°) and three tests were repeated for each direction. The true stress−strain curves of the zirconium alloys are displayed in Fig. 9. The mechanical properties such as yield strength (YS), ultimate tensile strength (UTS), the coefficient of the hardening rule (K), the Lankford value (r) as well as the hardening exponent (n_1) of the three sets of zirconium alloys are summarized in Table 2. The weighted average of r is noted as $\bar{r}$.

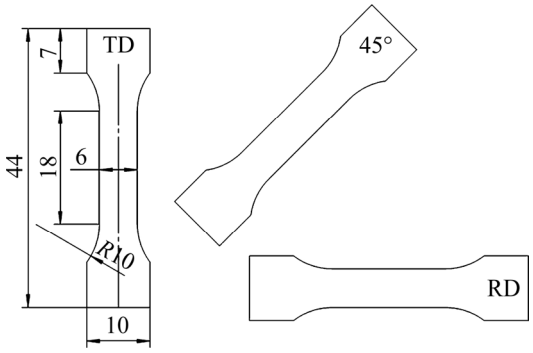

Fig. 8 Geometric dimensions of tensile samples (unit: mm)

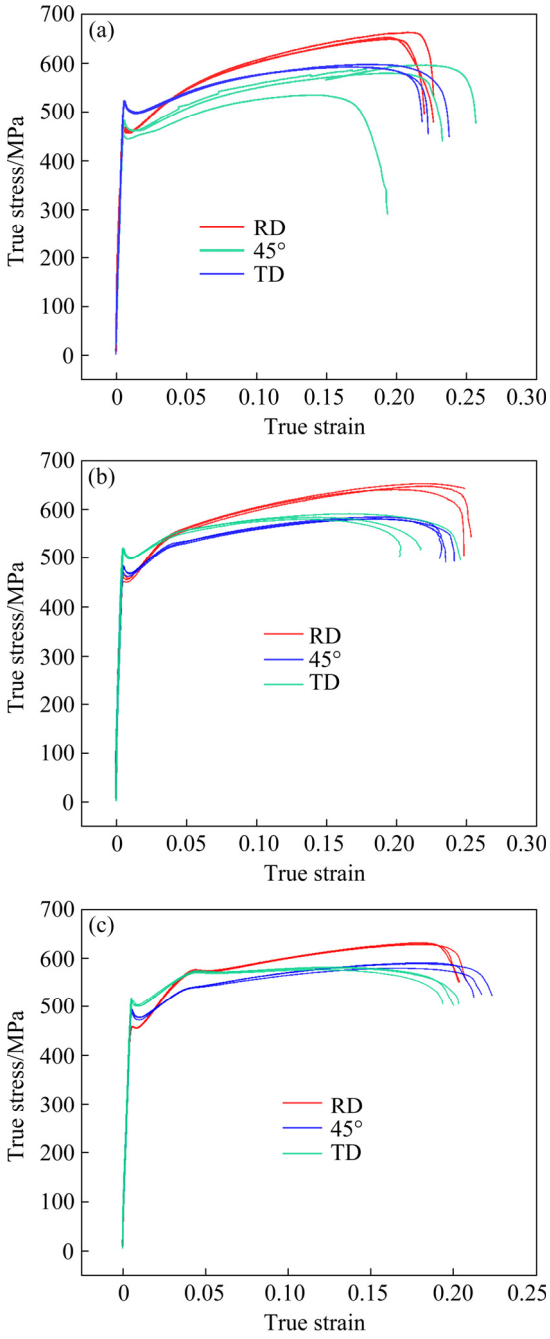

Fig. 9 True stress−true strain curves of as-received (a), AT I (b) and AT II (c) zirconium alloys

3.2 Construction of finite element model

It is known that for a specific structure, the formability of the sheet metal is related to not only the FLC of the material, but also the strain path during the forming process. To further quantitatively analyze the formability of the zirconium alloys, the concept of the forming margin field [38,39], which is noted as d and represents the minimum distance from the necking element to the FLC of material, is introduced in this study. To calculate the strain path of the necking element and explain the relationships between the forming margin field and the forming limit curve, the finite element method is employed. The finite element model of the clamping rigidity convexity is constructed by a commercial software Dynaform. During the calculation process, the punch and die structures are set as rigid bodies to ensure the calculation accuracy, and the minimum size of the mesh applied in this model is 0.1 mm.

Table 2 Mechanical properties of zirconium alloys

Material	Direction	YS/ MPa	UTS/ MPa	K/ MPa	r	$\overline{r}$	n_1
As-received	RD	452.8	548.0	856.0	3.827		0.150
	45	449.9	492.8	718.8	5.580	5.078	0.119
	TD	491.3	521.4	723.6	5.325		0.098
AT I	RD	451.9	545.9	932.6	3.019		0.164
	45	462.8	510.3	773.1	4.343	3.880	0.118
	TD	495.4	530.2	743.0	3.813		0.094
AT II	RD	481.2	549.5	851.3	3.011		0.127
	45	470.6	517.3	690.3	4.311	3.801	0.079
	TD	496.5	547.0	757.4	3.569		0.091

4 Results and discussion

4.1 FLCs of zirconium alloy sheets

The calculation results of FLCs by MK-Barlat method of the three kinds of zirconium alloys are shown in Fig. 10. It indicates that the FLCs of the as-received and the zirconium alloy under AT I are very close to each other while the one under AT I is slightly higher, which means that the formability of the zirconium alloy after AT I is slightly modified based on the as-received material. Besides, it can also be learnt from Fig. 10 that after the AT II, the FLC of the material declines sharply, which means that the formability of the zirconium alloy deteriorates through the AT II. Generally speaking, the higher the position the FLC is located in the strain coordinate, the larger the safety region the sheet metal possesses during the forming process. It is known that the FLC is an intrinsic property of materials to reflect the forming performance of materials. Therefore, from the results shown in Fig. 10, it can be indicated that the forming performance of the zirconium alloys can be modified through proper annealing treatments.

However, only the results of FLCs shown in Fig. 10 are not sufficient enough to explain the phenomenon of the stamping tests displayed in Figs. 2−4. It is known that for a specific structure, such as the clamping rigidity convexity used in this study, the crack is not only related to the FLC of the material but also to the strain path of the critical area with the highest cracking possibility. By using the same material, which means that the FLC is fixed, different strain paths may bring completely opposite forming results. Also, this is related to another concept, the forming limit margin field for a specific structure, which will be discussed later.

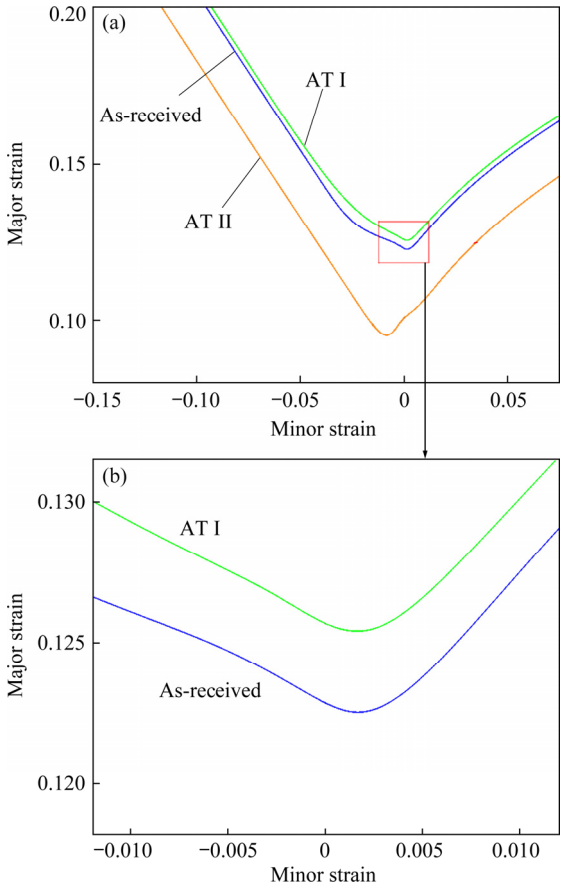

Fig. 10 FLCs of zirconium alloys calculated by MK-Barlat method

4.2 Strain path and forming limit margin field

The strain path of the necking element of the finite element model during the deformation of the clamping rigidity convexity, noted as element 15173, is shown in Fig. 11. From Fig. 11, it can be clearly seen that the strain paths of the three materials (as-received, AT I and AT II) are very close to each other and the annealing treatments have not significantly altered the strain paths of the zirconium alloys. However, combined with the results of strain paths and FLCs calculated before, the values of the forming limit margin field of the three materials can be derived and the results are quite different.

From Fig. 11(b), it can be captured that the strain path of the necking element is over the forming limit curve and the value of the forming limit margin field d_0=−0.35%, which indicates a crack risk for the necking area of the clamping rigidity convexity. While, it can be learnt

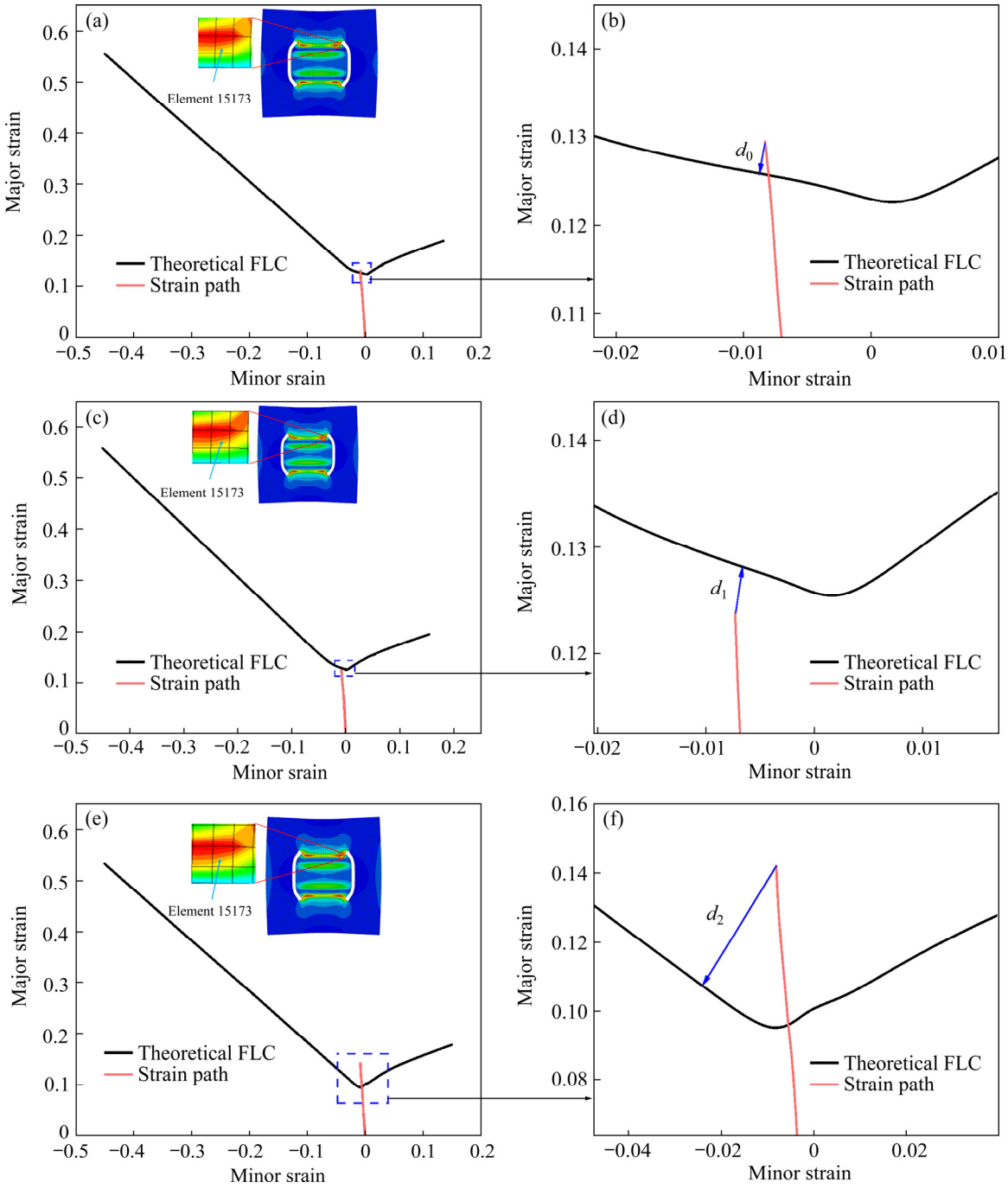

Fig. 11 Strain paths of necking element of as-received (a, b), AT I (c, d) and AT II (e, f) materials

from Fig. 11(d) that compared to the as-received material, the strain path of the necking element of the material after AT I remains in the safety area from the beginning to the end during the whole forming process. The margin field of the one after AT I is d_1=0.43%, which indicates that the formability of the material after this annealing treatment has been improved nearly twice. Particularly, it is worth noting that through the AT I, the forming performance improvement of the material has been a breakthrough from quantitative change to qualitative change, greatly impacting the overall forming yield of nuclear fuel assemblies. On the other hand, as for the zirconium under AT II, it can be seen from Fig. 11(f), the end of the strain path of the necking element far exceeds the forming limit curve and the corresponding value of the forming limit margin field d_2 is −2.8%, which means that there is a huge crack risk for the forming structure. The results of the strain paths and

forming limit margin fields of the materials have supported the physical phenomenon of the stamping experiments mentioned in Section 2.

From above, it can be deduced that the value of the forming limit margin field is related to both of the forming limit curve of material and the strain path of the necking element of the specific structure. The strain path can be changed by the geometric structure of the forming part, forming processing parameters (such as punch speed and blanker holder force) and the material properties, while the forming limit curve is all about material. However, in this study, the boundary conditions of the geometric structure of the forming part and the punching processing parameters remain exactly the same during the stamping experiments shown in Fig. 2 to Fig. 4. Therefore, the differences of the forming limit margin fields of the three materials should be intrinsically attributed to the changes of the material characters by annealing treatments.

4.3 Microstructures and textures of zirconium alloys

The grain maps of the Zr−Sn−Nb zirconium alloys with different annealing treatments are illustrated in Fig. 12. The grain sizes of the as-received material, AT I and AT II are 2.04, 1.84 and 2.28 μm, respectively. From Fig. 12 it can be learnt that after the AT I, the grain size of the Zr−Sn−Nb zirconium alloy is the smallest among the three specimens. This phenomenon could be attributed to the fact that the annealing temperature of the AT I is lower than that of the as-received material and a lower annealing temperature is beneficial to the grain refinement [40]. While, as the annealing temperature increases to 620 °C, which is the case of the AT II, the fine grains continue to grow after the annealing treatment, resulting in an increase in the average grain size. It is known that the refined grain enhances the forming performance of the sheet metal. For the cases in this study, after the AT I, the grain size of the material is refined and the average value of hardening exponent n is improved to 0.125, thus resulting in the rise of the FLC shown in Fig. 10. Accordingly, as the grain size continues to grow by an increasing annealing temperature employed by AT II, the average value of the hardening exponent n declines to 0.099, resulting in the fall of the FLC and the reduction of the forming margin field shown in Fig. 11(f).

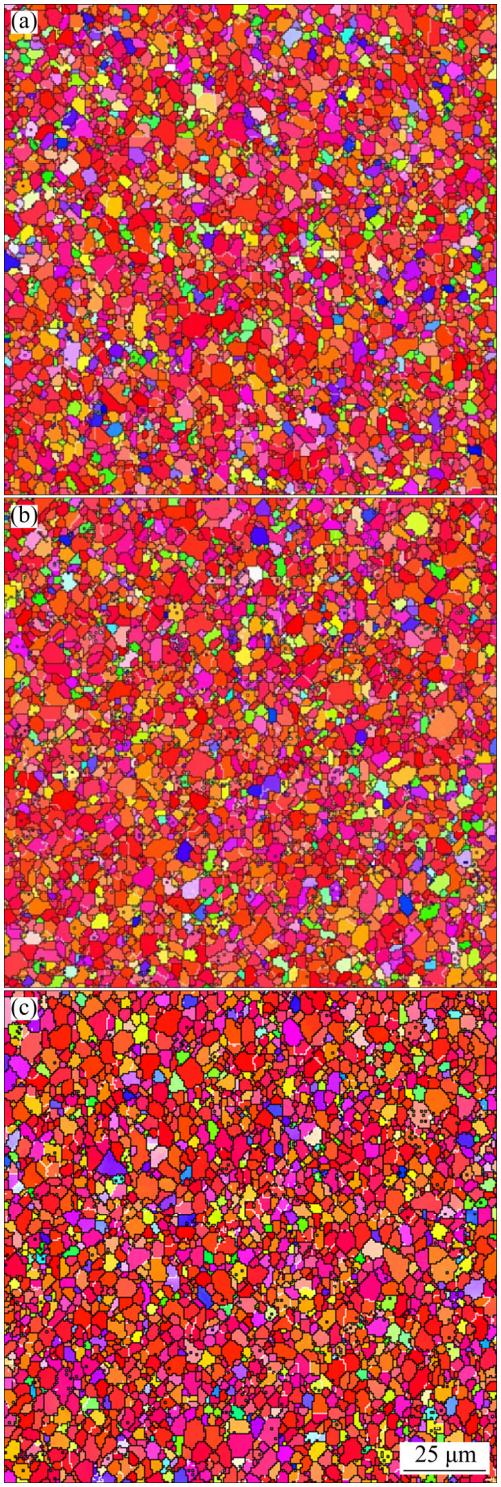

Fig. 12 Grain maps of as-received (a), AT I (b) and AT II (c) zirconium alloys

Moreover, from the pole figures displayed in Fig. 13, the maximum values of the base textures of the as-received, AT I and AT II materials are 6.49, 6.20 and 6.46, respectively. Therefore, it can be deduced from Fig. 13 that the evolution processes of recrystallization texture of the zirconium alloys

are changed by the annealing treatments. Compared with the as-received material, the total amount of the texture and the polar density of the zirconium alloys decrease for each of the annealing treatment. With the drop of the texture and the polar density, the anisotropy of the material, which reflects the weighted average of the Lankford value (r) in Table 2, is also reduced simultaneously for both of the annealing treatments. Furthermore, since a weakened base texture is beneficial to metal forming [41], the annealing treatment will help the Zr−Sn−Nb alloy to improve the forming performance.

Besides, the forming performance of the material is also related to the tendency of the crack extension during the plastic deformation process. From the study of JIN et al [42], the low-angle boundary and part of the high-angle boundary (the one with the misorientation less than 15°) have a better resistance to the cracking. Therefore, the misorientation distribution of the three zirconium alloys is obtained and shown in Fig. 14, and the

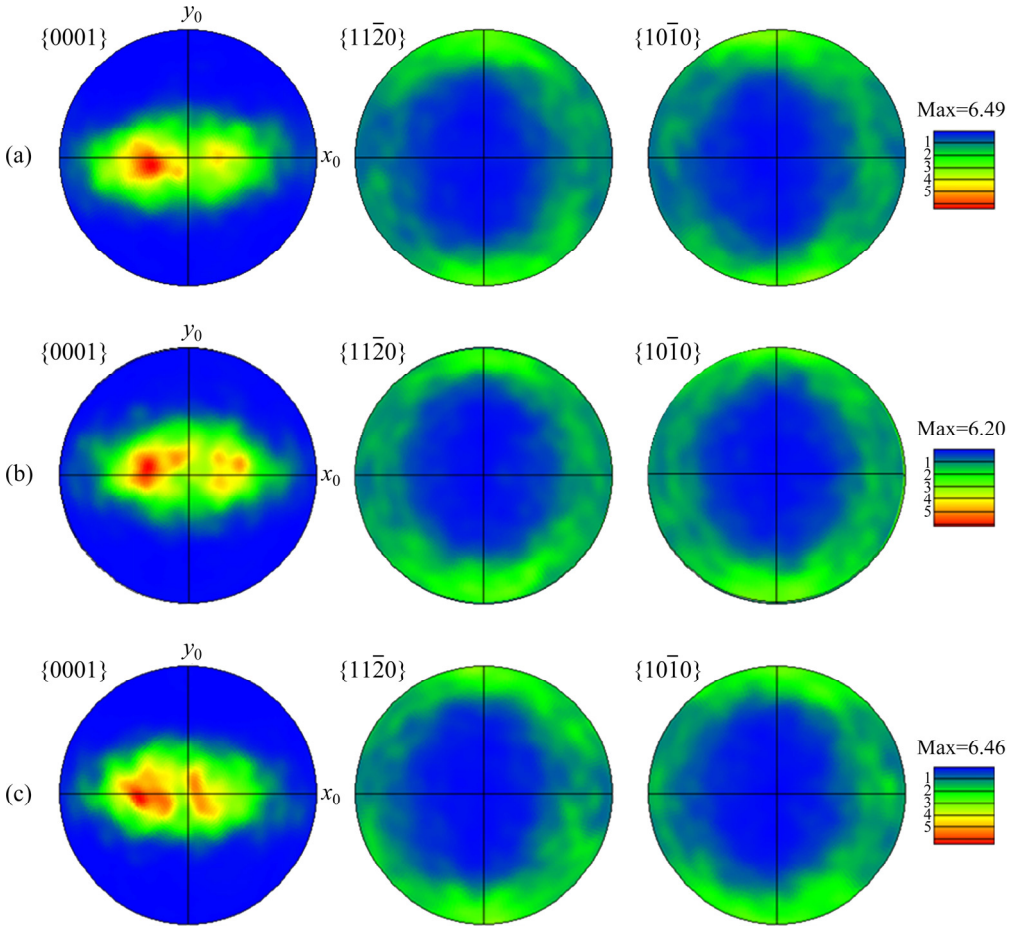

Fig. 13 Pole figures of as-received (a), AT I (b) and AT II (c) zirconium alloys

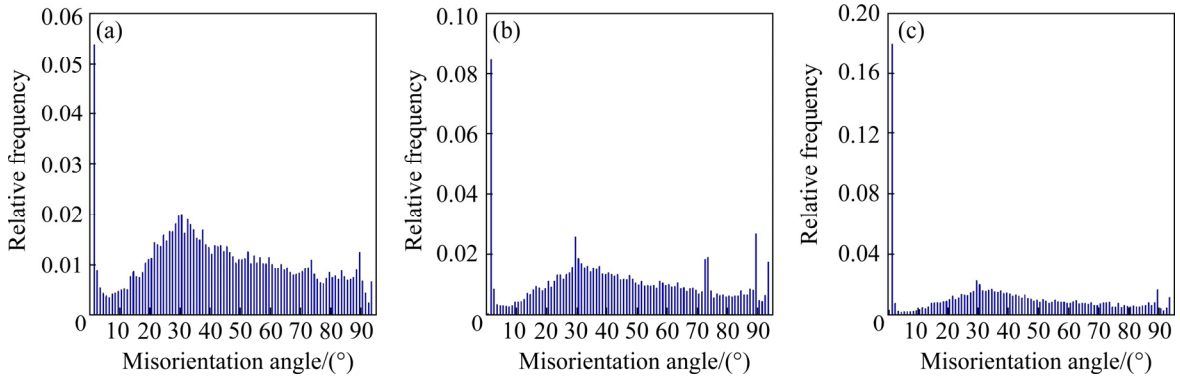

Fig. 14 Distribution of misorientation angles of as-received (a), AT I (b) and AT II (c) zirconium alloys

proportions of the low-angle boundary with the misorientation less than 15° results are illustrated in Fig. 15. From Fig. 15, it can be learnt that compared with the as-received material, both of the AT I and II samples occupy higher proportions in the area of boundary with misorientation angle less than 15°, which can explain why the forming limit curves of the as-received material and the material under AT I are very close to each other, but in the actual stamping experiments, the former one produces obvious cracks while the initial cracks have not extended continuously in the case of the latter. As for the material under AT II, even the low-angle boundary could help to resist the cracks, the grain size and the texture have limited the forming performance of the material, which could be seen from the FLCs shown in Fig. 10.

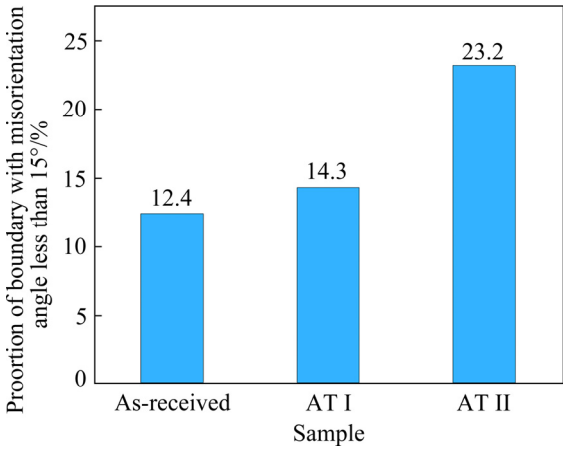

Fig. 15 Proportions of boundary with misorientation angle less than 15°

5 Conclusions

(1) The forming performances of the zirconium alloys are directly related to the annealing treatments. The number of the crack failure during the rigid convex stamping experiments of the alloys under ATI and AT II are 0 and 9, respectively, while that of the as-received material is 2. It should be attributed to the changes of the FLCs arising from the variations of the hardening exponents and the differences of the strain paths influenced by the misorientation distribution.

(2) Combined with the calculation results of the strain paths of the rigidity convexities and the position of the FLCs in the strain coordinate system, the forming limit margin fields of the necking element of the zirconium alloy under AT I and AT II are 0.43% and −2.8%, respectively, while that of the as-received alloy is −0.35%. This means that the forming performances of the zirconium alloys can be modified obviously by proper annealing treatments.

References

[1] VASNIN A M, GOL'TSEV V Y, MARKOCHEV V M, RIVKIN E Y. Resistance to fracture of a zirconium alloy containing 2.5% Nb [J]. Strength of Materials, 1974, 6(12): 1535−1539.

[2] KOLESNIK M, ALIEV T, LIKHANSKII V. The modeling of the hydrogen solid solubility hysteresis in zirconium alloys [J]. Acta Materialia, 2019, 177: 131−140.

[3] JUNG Y I, LEE M H, CHOI B K, PARK J Y, JEONG Y H. Development of a manufacturing process for Zr-based spacer grid materials [J]. Journal of Nuclear Materials, 2009, 392(3): 482−486.

[4] TERRANI K A. Accident tolerant fuel cladding development: Promise, status, and challenges [J]. Journal of Nuclear Materials, 2018, 501: 13−30.

[5] AL-OLAYYAN Y, FUCHS G E, BANEY R, TULENKO J. The effect of Zircaloy-4 substrate surface condition on the adhesion strength and corrosion of SiC coatings [J]. Journal of Nuclear Materials, 2005, 346(2/3): 109−119.

[6] NOUDURU S K, MANDAPAKA K K, ROYCHOWDHURY S, GUMMA S, SHARMA R, VERMA R, KAIN V. Nodular corrosion of zirconium alloys in gaseous environment containing different contaminants [J]. Journal of Nuclear Materials, 2021, 545: 152640.

[7] HE Wei-jun, CHEN Xin, LIU Qing. Effect of pre-annealing deformation on thermally activated twin boundary migration in a zirconium alloy [J]. Journal of Alloys and Compounds, 2018, 742: 29−37.

[8] XIA C Q, FENG Z H, YANG Y H, ZHANG Z G, JING R, PAN B, ZHANG X Y, MA M Z, LIU R P. Microstructure and corrosion behavior of the annealed Zr−40Ti−5Al−4V alloys [J]. Journal of Alloys and Compounds, 2016, 666: 301−308.

[9] SHI Yin-dong, ZHANG Guo-sheng, LI Ming, GUO De-feng, ZHANG Zhi-xiao, WEI Bing-ning, LI Jing-tao, ZHANG Xiang-yi. Effect of heat treatment on the microstructure and tensile properties of deformed α/β Ti−47Zr−5Al−3V alloy [J]. Journal of Alloys and Compounds, 2016, 665: 1−6.

[10] XIAO Jian-xiong, CHEN Zhi-yong, SHAO Jian-bo, CHEN Tao, LIN Xia, LIU Chu-ming. Evolution of long-period stacking ordered phases and their effect on recrystallization in extruded Mg−Gd−Y−Zn−Zr alloy during annealing [J]. Materials Characterization, 2020, 167: 110515.

[11] POYRAZ O, ÖGEL B. Recrystallization, grain growth and austenite formation in cold rolled steels during intercritical annealing [J]. Journal of Materials Research and Technology, 2020, 9(5): 11263−11277.

[12] HE Wei-jun, CHEN Xin, LIU Na, LUAN Bai-feng, YUAN Gai-huan, LIU Qing. Cryo-rolling enhanced inhomogeneous deformation and recrystallization grain growth of a

zirconium alloy [J]. Journal of Alloys and Compounds, 2017, 699: 160−169.

[13] CHEN Yu, JIANG Jian-zhong. Formation of the *B*2-ZrCo phase and micro-hardness evolution in Zr−Co−Al BMGs via conventional and flash annealing [J]. Journal of Alloys and Compounds, 2020, 834: 154230.

[14] MAITY S, SANYAL S, CHAKRABORTY S, SINHA A, BERA S. Effect of Nb content on the evolution of *β*-Zr and Mo_2Zr phase in Zr−Nb−Mo alloy during high energy ball milling and annealing [J]. Journal of Alloys and Compounds, 2019, 777: 397−405.

[15] ROGACHEV S O, NIKULIN S A, KHATKEVICH V M, GORSHENKOV M V, SUNDEEV R V, VELIGZHANIN A A. Effect of annealing on structural and phase transformations and mechanical properties of ultrafine-grained E125 zirconium alloy obtained by high-pressure torsion [J]. Materials Letters, 2017, 206: 26−29.

[16] HE Wei-jun, CHAPUIS A, CHEN Xin, LIU Qing. Effect of loading direction on the deformation and annealing behavior of a zirconium alloy [J]. Materials Science and Engineering A, 2018, 734: 364−373.

[17] TIAN Hang, WANG Xi-tao, GONG Wei-jia, ZHOU Jun, ZHANG Hai-long. Recrystallization behavior of cold-rolled Zr−1Nb alloy [J]. Journal of Nuclear Materials, 2015, 456: 321−328.

[18] ZHANG Zi-chen, WANG Ri-chu, PENG Chao-qun, FENG Yan, WANG Xiao-feng, WU Xiang, CAI Zhi-yong. Effect of elevated-temperature annealing on microstructureand properties of Cu−0.15Zr alloy [J]. Transactions of Nonferrous Metals Society of China, 2021, 31(12): 3772−3784.

[19] TIAN Yuan, MIAO Hong-wei, NIU Jia-lin, HUANG Hua, KANG Bin, ZENG Hui, DING Wen-jiang, YUAN Guang-yin. Effects of annealing on mechanical properties and degradation behavior of biodegradable JDBM magnesium alloy wires [J]. Transactions of Nonferrous Metals Society of China, 2021, 31(9): 2615−2625.

[20] KAMALI M R, MASHREGHI A R, KARJALAINEN L P, HASANI S, JAVAHERI V, SEIYEDBEIGI M, KÖMI J. Impact of annealing treatment on the microstructural-dependent mechanical properties of a cold-rolled Fe−Co−10V alloy [J]. Materials Science and Engineering A, 2021, 821: 141595.

[21] HUANG Yu-feng, LIU Wen-sheng, MA Yun-zhu, TANG Si-wei, CHEN Bai-shan. Effect of annealing treatment on the microstructure and mechanical properties of hot compression $Au_{80}Sn_{20}$ alloy [J]. Materials Science and Engineering A, 2018, 722: 69−75.

[22] CHEN Le, YANG Zhong-bo, QIU Jun, LIANG Bo, LI Wei-jun, HONG Xiao-feng, WANG Lian. Effect of heat treatment on tensile properties and microstructure of new domestic zirconium alloys [J]. Nuclear Power Engineering, 2017, 38(6): 129−133. (in Chinese)

[23] GENSAMER M. Strength and ductility [J]. Metallography, Microstructure, and Analysis, 2017, 6(2): 171−185.

[24] BANABIC D, KAMI A, COMSA D S, EYCKENS P. Developments of the Marciniak−Kuczynski model for sheet metal formability: A review [J]. Journal of Materials Processing Technology, 2021, 287: 116446.

[25] KEELER S P. Plastic instability and fracture in sheets stretched over rigid punches [D]. Series: Massachusetts Institute of Technology, 1961.

[26] KEELER S P. Determination of forming limits in automotive stampings [C]//SAE Technical Paper Series, Warrendale: SAE International, 1965.

[27] GOODWIN G M. Application of strain analysis to sheet metal forming problems in the press shop [J]. SAE Transactions, 1968, 77: 380−387.

[28] DIZAJI S A, DARENDELILER H, KAFTANOĞLU B. Prediction of forming limit curve at fracture for sheet metal using new ductile fracture criterion [J]. European Journal of Mechanics - A/Solids, 2018, 69: 255−265.

[29] MA B L, LIU Z G, JIANG Z, WU X D, DIAO K S, WAN M. Prediction of forming limit in DP590 steel sheet forming: An extended fracture criterion [J]. Materials & Design, 2016, 96: 401−408.

[30] BANABIC D. Multiscale modelling in sheet metal forming [M]. Heideberg: Springer, 2016.

[31] LEI Cong-yi, MAO Jian-zhong, ZHANG Xiao-min, LIU Jing-xuan, WANG Lian, CHEN Ding. A comparison study of the yield surface exponent of the Barlat yield function on the forming limit curve prediction of zirconium alloys with M−K method [J]. International Journal of Material Forming, 2021, 14(3): 467−484.

[32] MARCINIAK Z, KUCZYŃSKI K. Limit strains in the processes of stretch-forming sheet metal [J]. International Journal of Mechanical Sciences, 1967, 9(9): 609−620.

[33] HUTCHINSON J W, NEALE K W, NEEDLEMAN A. Sheet Necking—I. Validity of plane stress assumptions of the long-wavelength approximation [J]. Mechanics of Sheet Metal Forming Plenum, 1978, 77: 111−126.

[34] HUTCHINSON J W, NEALE K W. Sheet Necking—II. Time-independent behavior [J]. Mechanics of Sheet Metal Forming Plenum, 1978, 77: 127−153.

[35] BARLAT F, LIAN K. Plastic behavior and stretchability of sheet metals. Part I: A yield function for orthotropic sheets under plane stress conditions [J]. International Journal of Plasticity, 1989, 5(1): 51−66.

[36] BANABIC D. Sheet metal forming processes springer [M]. Heidelberg: Springer, 2010.

[37] HOSFORD W F. Comments on anisotropic yield criteria [J]. International Journal of Mechanical Sciences, 1985, 27(7): 423−427.

[38] WEI Dong-lai, CUI Zhen-shan, CHEN Jun. Optimization and tolerance prediction of sheet metal forming process using response surface model [J]. Computational Materials Science, 2008, 42(2): 228−233.

[39] CUI Jun-jia, HU Ming, LI Guang-yao. Establishment and applications of thermal forming limit margin field graph for automobile components [J]. China Mechanical Engineering, 2017, 28(3): 358−365. (in Chinese)

[40] ZHU Guang-wei, ZHAO Yi-cheng, ZHAO Fan, QI Peng, ZHANG Zhi-hao. Effect of stress annealing on texture and recrystallization behavior of Zr-4 alloy [J]. Chinese Journal of Engineering, 2020, 42(9): 1174−1181. (in Chinese)

[41] ZHANG Hua, REN Shui-ai, LI Xia, WANG Li-fei, FAN Jian-feng, CHEN Shui-ying, ZHU Li-long, MENG Fan-chao, TONG Yang, ROVEN H J, ZHANG Shang-zhou, JIANG

Liang. Dramatically enhanced stamping formability of Mg−3Al−1Zn alloy by weakening (0001) basal texture [J]. Journal of Materials Research and Technology, 2020, 9(6): 14742−14753.

[42] JIN Y J, LU H, YU C, XU J J. Study on grain boundary character and strain distribution of intergranular cracking in the CGHAZ of T23 steel [J]. Materials Characterization, 2013, 84: 216−224.

退火工艺对锆合金成形性能的影响

雷从一[1,2]，毛建中[1,2]，周惦武[1,2]，张小民[1,2]，王 练[3]

1. 湖南大学 汽车车身先进设计制造国家重点实验室，长沙 410082；
2. 湖南大学 机械与运载工程学院，长沙 410082；
3. 国核宝钛锆业股份公司, 宝鸡 721000

摘 要：研究退火工艺(ATs)对 Zr−Sn−Nb 合金带材显微组织的影响。基于核燃料组件用条带特征，进行冲制实验，并定量表征锆合金带材的成形性能。结果表明，580 ℃退火(AT I)样品、620 ℃退火样品(AT II)和原材的小角度晶界占比分别为 14.3%、23.2%和 12.4%。AT I 带材的成形极限裕度为 0.43%，而原材和 AT II 带材的成形裕度分别仅为−0.35%和−2.8%。退火工艺影响带材再结晶织构的演化过程和改变晶粒尺寸。由于织构总量和极密度变化与带材各向异性程度密切相关，小角度晶界影响带材冲制过程中颈缩单元的应变路径与裂纹扩展，而晶粒尺寸影响带材硬化指数。

关键词：成形性能；锆合金；退火工艺；应变路径；成形极限；织构

(Edited by Wei-ping CHEN)